



Anti-diffusion interface sharpening technique for two-phase compressible flow simulations

K.K. So ^{*}, X.Y. Hu, N.A. Adams

Institute of Aerodynamics and Fluid Mechanics, Technische Universität München, 85748 Garching, Germany

ARTICLE INFO

Article history:

Received 30 September 2011

Received in revised form 9 February 2012

Accepted 15 February 2012

Available online 3 March 2012

Keywords:

Anti-diffusion

Interface sharpening

Two-phase compressible flow

Volume-of-fluid

Shock-bubble interaction

ABSTRACT

In this paper we propose an interface sharpening technique for two-phase compressible-flow simulations based on volume-of-fluid methods. The idea of sharpening the two-fluid interface is to provide a correction algorithm which can be applied as post-processing to the volume-fraction field after each time step. For this purpose an anti-diffusion equation, i.e. a diffusion equation with a positive diffusion coefficient, is solved to counter-act the numerical diffusion resulting from the underlying VOF discretization. The numerical stability and volume-fraction boundedness in solving the anti-diffusion equation are ensured by a specified discretization scheme. No interface reconstruction and interface normal calculation are required in this method. All flow variables are updated with the sharpened volume-fraction field for ensuring the consistency of the variables, and the update of the phase mass, momentum and energy is conservative. Numerical results for shock-tube and shock-bubble interactions based on the ideal-gas EOS and shock contact problems based on the Mie–Grüneisen EOS show an improved interface resolution. The large-scale interface structures are in good agreement with reference results, and finer small-scale interface structures are recovered in a consistent manner as the grid resolution increases. As compared with reference high grid-resolution numerical results based on AMR algorithms, the interface roll-up phenomena due to the Richtmyer–Meshkov instability and the Kelvin–Helmholtz instability are recovered reliably for shock-bubble interactions involving different ideal gases.

© 2012 Elsevier Inc. All rights reserved.

1. Introduction

The impact of a shock wave on two-phase compressible flows is a fundamental topic in science and engineering. To better understand the instability phenomena that are important for the evolution of such flows, basic configurations, such as shock-bubble interactions [26] in two-phase compressible flows, are studied to investigate the Richtmyer–Meshkov instability [4], the Kelvin–Helmholtz instability and the mixing mechanisms in shock-accelerated flows [40]. Flows of this type are present in many engineering applications including supersonic mixing and combustion systems [43] and extra-corporeal shock-wave lithotripsy [26]. Two-phase compressible flows interacting with a shock wave have been studied extensively during the last decades, where in particular detailed numerical simulations help to elucidate the essential phenomena and interaction mechanisms [24,29,43,31,21].

In simulations the phase interface location is tracked explicitly or captured implicitly, where the approaches are front-tracking methods [39], level-set methods [7] and volume-of-fluid (VOF) methods [8]. Front-tracking methods follow explicitly

^{*} Corresponding author.

E-mail address: kai.so@aer.mw.tum.de (K.K. So).

the interface by means of marker points. Level-set methods capture the interface position by the zero-contour of the level-set function. VOF methods use the volume fraction to locate one phase in another phase. The interface position is captured by a diffused-interface representation, or located by an interface reconstruction algorithm. Different numerical methods were developed for different interface representation methods: among others the front-tracking/ghost-fluid method [39] for front-tracking representations; discontinuous Galerkin methods [44] or weighted essentially non-oscillatory (WENO) schemes [7,13,11] for level-set representations; volume tracking by means of an interface reconstruction [35], interface-compression method [33], and the anti-diffusive scheme [16] for VOF representations. Methods also worth noting for two-phase compressible flow simulations include the localized artificial diffusivity method for mass-fraction representations [38,15], the stratified flow model and AUSM⁺-up scheme [5], the γ -model [1,12,20], and the arbitrary Lagrangian–Eulerian scheme which involves a grid evolution [18].

The VOF volume-capturing method possesses the advantage of exact conservation properties, but suffers from numerical diffusion which causes two-fluid interfaces to smear. Specific numerical schemes to suppress or counter-act the numerical diffusion, and to maintain the interface sharpness in the course of simulations are thus desirable and essential for VOF methods. Previous works on maintaining a sharp interface without an interface reconstruction include the interface compression technique by [33] which originates from the interface compression technique for two-phase incompressible flows by [23], and the anti-diffusive numerical scheme based on a limited downwind strategy where stability and consistency criteria are proposed to make use of the downwind contribution [16].

In this paper, we propose an interface sharpening technique for two-phase compressible flow simulations based on VOF methods. The idea of sharpening the two-fluid interface is to provide a correction algorithm which can be applied as post-processing to the volume-fraction field after each time step. For such a purpose, an anti-diffusion equation is solved for counter-acting the numerical diffusion resulting from the underlying discretization. The interface-sharpening technique is modular and can be applied to general underlying VOF discretizations. No interface reconstruction is required to track the interface position. The technique originally has been developed and verified for two-phase incompressible flow simulations [37]. Compressible flows pose the particular challenge of ensuring consistency among the flow variables. It is the objective of this paper to present a further development of the method for two-phase compressible flows with numerical validation results and some applications as feasibility demonstration.

The paper is organized as follows. First, the governing equations for two-phase compressible flows adopted in the paper are described. Second, the underlying Riemann solver, the numerical method for the volume-fraction transport equation and in particular the numerical method for interface sharpening by solving an anti-diffusion equation are detailed. Special consideration is given to modifications of the incompressible formulation [37] necessary for compressible flows. Validation cases for different equations of state (EOS) and in 1 and 2 dimensions are presented to illustrate the improvement obtained by the interface sharpening method. Finally, an application of the method to a complex interaction problem is given for illustration.

2. Governing flow equations

Various mathematical models for two-phase compressible flow simulations have been developed with different sets of governing equations [14,32,17]. In this paper we consider a basic conservative formulation of the Euler equations assuming a single velocity and pressure equilibrium. The two phases are represented by the respective volume fractions, where the formulation of the volume-fraction transport equations of [8] is adopted. This volume-fraction transport equation formulation has been extensively studied by [19] for simulations with the ideal-gas EOS and the Mie–Grüneisen EOS [27], and has been employed for a computational study of shock-bubble interactions of different gas pairs and at different shock speeds by [21]. With two mass conservation equations, one momentum conservation equation and one energy conservation equation a six-equation model is obtained as follows:

$$\frac{\partial \alpha}{\partial t} + \nabla \cdot \alpha \mathbf{u} = \alpha \frac{\bar{K}_s}{K_s^\alpha} \nabla \cdot \mathbf{u}, \quad (1)$$

$$\frac{\partial \beta}{\partial t} + \nabla \cdot \beta \mathbf{u} = \beta \frac{\bar{K}_s}{K_s^\beta} \nabla \cdot \mathbf{u}, \quad (2)$$

$$\frac{\partial \alpha \rho^\alpha}{\partial t} + \nabla \cdot \alpha \rho^\alpha \mathbf{u} = 0, \quad (3)$$

$$\frac{\partial \beta \rho^\beta}{\partial t} + \nabla \cdot \beta \rho^\beta \mathbf{u} = 0. \quad (4)$$

$$\frac{\partial \rho \mathbf{u}}{\partial t} + \nabla \cdot \rho \mathbf{u} \mathbf{u} + \nabla p = 0, \quad (5)$$

$$\frac{\partial \rho E}{\partial t} + \nabla \cdot (\rho E + p) \mathbf{u} = 0, \quad (6)$$

where α and β are the volume fractions of the two phases respectively, t is the time, \mathbf{u} is the velocity, \bar{K}_s is the mixture bulk modulus, K_s^α and K_s^β are the phase bulk moduli, ρ^α and ρ^β are the phase densities, p is the pressure and E is the total energy.

It should be noted that, instead of solving Eq. (2), β can be computed directly from α based on the relation $\alpha + \beta = 1$. Here we keep the original form of the volume-fraction transport Eqs. (1) and (2) as adopted in [8] for demonstrating the modularity of the interface sharpening method and the applicability of the method to general underlying VOF discretizations.

As the formulation of the volume-fraction transport equations are capable of simulations with the ideal-gas EOS and the Mie–Grüneisen EOS as studied in [8,19,21], in this paper we also consider these two EOS as examples. The ideal-gas EOS reads

$$p(\rho, e) = (\gamma - 1)\rho e, \quad (7)$$

where γ is the ratio of specific heats and e is the internal energy. The Mie–Grüneisen EOS reads

$$p(\rho, e) = p_{\text{ref}} + \Gamma(\rho)\rho(e - e_{\text{ref}}), \quad (8)$$

where $p_{\text{ref}} = \rho_0 c_0^2 \eta / (1 - s\eta)^2$, $\eta = 1 - (\rho_0/\rho)$, $\Gamma(\rho) = \Gamma_0 \rho_0 / \rho$, $e_{\text{ref}} = 0.5 p_{\text{ref}} \eta / \rho_0$ and ρ_0 , c_0 , s , Γ_0 are constant coefficients.

A general EOS can be formulated to represent both the ideal-gas EOS and the Mie–Grüneisen EOS. The general EOS for each phase reads

$$p^k(\rho^k, e^k) = \Gamma^k(\rho^k)\rho^k e^k + f^k(\rho^k), \quad (9)$$

where $\Gamma^k(\rho^k)$ and $f^k(\rho^k)$ are functions of ρ^k , and the superscript k denotes the phase, i.e. α or β .

By assuming pressure equilibrium, i.e. $p^\alpha = p^\beta$, p can be calculated by

$$p(\rho, e, \alpha, \beta) = \frac{\rho e + \left(\frac{\alpha f^\alpha(\rho^\alpha)}{\Gamma^\alpha(\rho^\alpha)} + \frac{\beta f^\beta(\rho^\beta)}{\Gamma^\beta(\rho^\beta)} \right)}{\left(\frac{\alpha}{\Gamma^\alpha(\rho^\alpha)} + \frac{\beta}{\Gamma^\beta(\rho^\beta)} \right)}. \quad (10)$$

3. Numerical methods

3.1. Riemann solver

We point out that the particular choice of Riemann solver serves as example for using the interface-sharpening method which can be formulated for other Riemann solvers in a straight-forward way.

The HLL Riemann solver [41] is adopted for calculating the numerical flux at cell face, \mathbf{F}_{HLL} ,

$$\mathbf{F}_{\text{HLL}} = \begin{cases} \mathbf{F}_L & \text{if } 0 \leq S_L, \\ \frac{S_R \mathbf{F}_L - S_L \mathbf{F}_R + S_L S_R (\mathbf{U}_R - \mathbf{U}_L)}{S_R - S_L} & \text{if } S_L \leq 0 \leq S_R, \\ \mathbf{F}_R & \text{if } 0 \geq S_R, \end{cases} \quad (11)$$

where $\mathbf{U} = (\alpha, \beta, \alpha\rho^\alpha, \beta\rho^\beta, \rho\mathbf{u}, \rho E)$ is the vector of the cell-averaged conserved variables, \mathbf{F} is the cell-average flux, S is the bound of the fastest signal velocity, and the subscripts L and R denote the variables at the cell face computed by the reconstructed values at the two sides of the cell face.

The lower and upper bounds of the fastest signal velocities are calculated by

$$S_L = \min(u_L - a_L, u_R - a_R), \quad S_R = \max(u_L + a_L, u_R + a_R), \quad (12)$$

where u_L and u_R are the flow velocity at the cell face, a_L and a_R are the mixture sound speeds at the cell face. The Wood formula or the frozen speed of sound [32] can be used for calculating a_L and a_R , and the latter is adopted in this paper as our results do not show significant differences for both:

$$a_L = \sqrt{\frac{(\alpha\rho^\alpha)_L}{\rho_L} (c_L^\alpha)^2 + \frac{(\beta\rho^\beta)_L}{\rho_L} (c_L^\beta)^2}, \quad a_R = \sqrt{\frac{(\alpha\rho^\alpha)_R}{\rho_R} (c_R^\alpha)^2 + \frac{(\beta\rho^\beta)_R}{\rho_R} (c_R^\beta)^2}, \quad (13)$$

where c_L^α , c_R^α , c_L^β and c_R^β are the phase sound speeds at the cell face computed based on the respective EOS.

3.2. Volume-fraction transport equations

The numerical method for solving the volume-fraction transport Eqs. (1) and (2) is detailed in [8,19] and illustrated below.

The volume fractions are updated in two steps. First the volume-fraction transport equations without the source terms are solved:

$$\frac{\partial \alpha}{\partial t} + \nabla \cdot \alpha \mathbf{u} = 0, \quad (14)$$

$$\frac{\partial \beta}{\partial t} + \nabla \cdot \beta \mathbf{u} = 0. \quad (15)$$

We denote the solutions of Eqs. (14) and (15) respectively as α^* and β^* which are the intermediate states. Then the compressibility effect represented by the source term is taken into account for the final solution:

$$\alpha^{n+1} = \alpha^* \left[1 + \left(\frac{\bar{K}_S}{K_S^\alpha} [1 - (\alpha^* + \beta^*)] \right) \right], \quad (16)$$

$$\beta^{n+1} = \beta^* \left[1 + \left(\frac{\bar{K}_S}{K_S^\beta} [1 - (\alpha^* + \beta^*)] \right) \right], \quad (17)$$

where α^{n+1} and β^{n+1} are the volume fractions at the new time step.

The numerical method ensures the relation $\alpha + \beta = 1$ during the evolution of the volume fractions. As mentioned in Section 2, instead of solving Eqs. (15) and (17), β^{n+1} can be computed directly from α^{n+1} based on the relation $\alpha + \beta = 1$ which holds for all time steps.

3.3. Anti-diffusion interface sharpening

The idea of sharpening the two-fluid interfaces is to provide a correction algorithm which can be applied as post-processing to the volume-fraction field after each time step. For such, an anti-diffusion equation, i.e. a diffusion equation with a positive diffusion coefficient, is solved to counter-act the numerical diffusion:

$$\frac{\partial \alpha}{\partial \tau} = -\nabla \cdot (D \nabla \alpha), \quad (18)$$

where $D > 0$ is an anti-diffusion coefficient and τ is a pseudo time.

A special discretization scheme is employed to ensure the numerical stability and the volume-fraction boundedness in solving the anti-diffusion equation. The solution procedure is described in [37]. Here, we focus on recapitulating the essential points in solving the anti-diffusion equation and detailing the differences from the incompressible formulation. First, the limited cell-averaged value of the gradient of α , $(\nabla \alpha)_{lim}$, is obtained by the regularization based on a minmod limiter. Then, the anti-diffusion flux for α , F_{AD}^α , at the cell face between cell P and cell N is obtained by:

$$F_{AD}^\alpha = \begin{cases} -D((\nabla \alpha)_{lim})_P \cdot \mathbf{S} & \text{if } |((\nabla \alpha)_{lim})_P| \leq |((\nabla \alpha)_{lim})_N|, \\ -D((\nabla \alpha)_{lim})_N \cdot \mathbf{S} & \text{if } |((\nabla \alpha)_{lim})_N| < |((\nabla \alpha)_{lim})_P|, \end{cases} \quad (19)$$

where $((\nabla \alpha)_{lim})_P$ and $((\nabla \alpha)_{lim})_N$ are the respective limited cell-averaged value of the gradient in cell P and cell N , \mathbf{S} is the cell face area vector which points from cell P to cell N .

The right-hand-side of Eq. (18) is calculated by

$$\nabla \cdot (-D(\nabla \alpha)) = \frac{\sum_{cf} (F_{AD}^\alpha)}{V}, \quad (20)$$

where \sum_{cf} denotes the summation over all cell faces and V is the cell volume.

The volume fraction is advanced in pseudo time by an explicit Euler scheme:

$$\alpha^{N+1} = \alpha^N + \nabla \cdot (-D(\nabla \alpha^N)) \Delta \tau \quad (21)$$

with N being the pseudo time index, and the time step limit on pseudo time,

$$\Delta \tau = \frac{1}{4} \frac{(\Delta x_{min})^2}{D}, \quad (22)$$

where Δx_{min} is the minimum cell width.

In the following we denote by $(\cdot)^{AD}$ a quantity that is obtained after applying the sharpening procedure. It should be noted that the anti-diffusion equation does not need to be integrated up to a certain pseudo time. Rather a certain number of iterations is performed to achieve a desired interface steepness, which is controlled by a stopping criterion detailed below. While other time-integration schemes can be used for the solution of the anti-diffusion equation, the explicit Euler scheme is employed here for its low computational cost.

As the anti-diffusion equation is meant to counter-act the numerical diffusion resulting from the volume-fraction transport, the choice of D is based on an estimation of the numerical diffusion of the underlying numerical scheme. Following the formulation of the HLL Riemann solver, D is chosen to be

$$D = \left| \frac{S_L S_R (\alpha_R - \alpha_L)}{S_R - S_L} \right|. \quad (23)$$

After α has been sharpened, all other flow variables in the governing equations have to be updated to ensure the consistency across the flow variables which is important for simulating the correct flow physics. As demonstrated in [33] where the interface compression technique is applied, in case only the interface function is compressed without updating the other flow variables, the mismatch of the compressed interface function and the smeared density field leads to an incorrect

interface evolution. To update the other flow variables the authors in [33] employ a hyperbolic function together with their interface compression technique for the mass conservation equation to localize the compression to the interface region. For the momentum and energy field, they first compute the primitive variables before applying the interface compression technique, and based on these primitive variables and the compressed interface function they estimate the new conserved variables. It is noted that based on this approach the compression in the interface function equation and in the mass conservation equation is not exactly consistent, and the update of the momentum and energy field is not conservative. Alternatively in our work, all the flow variables are updated according to α^{AD} for ensuring the consistency. For each time the α field is sharpened by solving an anti-diffusion equation, the other flow variables β , $\alpha\rho^\alpha$, $\beta\rho^\beta$, $\rho\mathbf{u}$, ρE are updated accordingly by respective flux defined based on F_{AD}^α . We denote these fluxes to update the other variables as F_{AD}^β , $F_{AD}^{\alpha\rho^\alpha}$, $F_{AD}^{\beta\rho^\beta}$, $F_{AD}^{\rho\mathbf{u}}$, $F_{AD}^{\rho E}$, respectively for the flow variables β , $\alpha\rho^\alpha$, $\beta\rho^\beta$, $\rho\mathbf{u}$, ρE .

To preserve the relation $\alpha + \beta = 1$, F_{AD}^β is defined as:

$$F_{AD}^\beta = -F_{AD}^\alpha. \quad (24)$$

$F_{AD}^{\alpha\rho^\alpha}$, $F_{AD}^{\beta\rho^\beta}$ are defined based on F_{AD}^α and F_{AD}^β , and the flow variables α , β , $\alpha\rho^\alpha$, $\beta\rho^\beta$ interpolated at cell face:

$$F_{AD}^{\alpha\rho^\alpha} = F_{AD}^\alpha \rho_f^\alpha, \quad (25)$$

$$F_{AD}^{\beta\rho^\beta} = -F_{AD}^\alpha \rho_f^\beta, \quad (26)$$

$$\rho_f^\alpha = \frac{(\alpha\rho^\alpha)_f}{\alpha_f}, \quad \rho_f^\beta = \frac{(\beta\rho^\beta)_f}{\beta_f}, \quad (27)$$

$$(\cdot)_f = \frac{(\cdot)_p d_N + (\cdot)_N d_p}{d_p + d_N}, \quad (28)$$

where $(\cdot)_p$ and $(\cdot)_N$ are the cell-averaged variables in cell P and N , d_p and d_N are the distances from the cell centers P and N to the respective cell-face centers, and $(\cdot)_f$ denotes the reconstruction at the cell face of the variables.

$F_{AD}^{\rho\mathbf{u}}$ is defined based on $F_{AD}^{\alpha\rho^\alpha}$, $F_{AD}^{\beta\rho^\beta}$, and the flow variables $\alpha\rho^\alpha$, $\beta\rho^\beta$, $\rho\mathbf{u}$ interpolated at cell face:

$$F_{AD}^{\rho\mathbf{u}} = (F_{AD}^{\alpha\rho^\alpha} + F_{AD}^{\beta\rho^\beta}) \frac{(\rho\mathbf{u})_f}{(\alpha\rho^\alpha)_f + (\beta\rho^\beta)_f}, \quad (29)$$

which can be rewritten to

$$F_{AD}^{\rho\mathbf{u}} = F_{AD}^\alpha (\rho_f^\alpha - \rho_f^\beta) \frac{(\rho\mathbf{u})_f}{(\alpha\rho^\alpha)_f + (\beta\rho^\beta)_f}. \quad (30)$$

$F_{AD}^{\rho E}$ is defined based on the assumption of pressure equilibrium. Given the phase EOS based on Eq. (9)

$$p^\alpha = \Gamma^\alpha (\rho e)^\alpha + f^\alpha, \quad (31)$$

$$p^\beta = \Gamma^\beta (\rho e)^\beta + f^\beta \quad (32)$$

and the pressure-equilibrium EOS Eq. (10),

$$p = \frac{\rho e + \left(\frac{\alpha f^\alpha}{\Gamma^\alpha} + \frac{\beta f^\beta}{\Gamma^\beta} \right)}{\left(\frac{\alpha}{\Gamma^\alpha} + \frac{\beta}{\Gamma^\beta} \right)}, \quad (33)$$

$F_{AD}^{\rho E}$ is obtained by imposing $p^\alpha = p = p^\beta$:

$$F_{AD}^{\rho E} = F_{AD}^\alpha [(\Gamma(\rho e))_f + f_f + (\rho E_k)_f], \quad (34)$$

$$(\Gamma(\rho e))_f = \left(\frac{\Gamma_f^\beta - \Gamma_f^\alpha}{\alpha_f \Gamma_f^\beta + \beta_f \Gamma_f^\alpha} \right) \left((\rho E)_f - \frac{\frac{1}{2} |(\rho\mathbf{u})_f|^2}{(\alpha\rho^\alpha)_f + (\beta\rho^\beta)_f} \right), \quad (35)$$

$$f_f = \left(\frac{f_f^\beta - f_f^\alpha}{\alpha_f \Gamma_f^\beta + \beta_f \Gamma_f^\alpha} \right), \quad (36)$$

$$(\rho E_k)_f = \left(\frac{\frac{(\alpha\rho^\alpha)_f}{\alpha_f} - \frac{(\beta\rho^\beta)_f}{\beta_f}}{(\alpha\rho^\alpha)_f + (\beta\rho^\beta)_f} \right) \left(\frac{\frac{1}{2} |(\rho\mathbf{u})_f|^2}{(\alpha\rho^\alpha)_f + (\beta\rho^\beta)_f} \right). \quad (37)$$

For cases with the ideal-gas EOS it is $f_f = 0$. It can be seen that F_{AD}^β , $F_{AD}^{\alpha\rho^\alpha}$, $F_{AD}^{\beta\rho^\beta}$, $F_{AD}^{\rho\mathbf{u}}$, $F_{AD}^{\rho E}$ are all defined based on F_{AD}^α and the flow variables interpolated at the cell face. Note that, as the relation $\alpha + \beta = 1$ always holds, F_{AD}^β can be calculated first instead of F_{AD}^α , and F_{AD}^α , $F_{AD}^{\alpha\rho^\alpha}$, $F_{AD}^{\beta\rho^\beta}$, $F_{AD}^{\rho\mathbf{u}}$, $F_{AD}^{\rho E}$ can be calculated based on F_{AD}^β in a similar fashion as illustrated above. Both solution procedures give the same set of anti-diffusion sharpening flux since $\nabla\alpha = -\nabla\beta$.

The variables $\beta, \alpha\rho^\alpha, \beta\rho^\beta, \rho\mathbf{u}, \rho E$ are then updated in the same way as α according to Eqs. (20) and (21) based on the above $F_{AD}^\beta, F_{AD}^{\alpha\rho^\alpha}, F_{AD}^{\beta\rho^\beta}, F_{AD}^{\rho\mathbf{u}}, F_{AD}^{\rho E}$ with the same pseudo time step. It should be noted that the formulation of the anti-diffusion sharpening flux for phase mass, momentum and energy is conservative.

The anti-diffusion equation can be solved repeatedly to attain an even sharper profile. A case- and grid-independent stopping criterion (i.e. no explicit dependence on fluid or geometry parameter and no explicit dependence on cell-size measurement) based on the measurement of the tolerance of the interface sharpness, TOL , as developed in [37] is employed to terminate the sharpening iterations:

$$TOL \geq \frac{\sum_i |(\nabla \cdot (\overline{\nabla \alpha})_{lim})| V_i}{\sum_i |((\overline{\nabla \alpha})_{CD})|^2 V_i}, \quad (38)$$

where \sum_i denotes the summation over all cells, the subscript i indicates the cell index, and V_i is the volume of the cell i . One can see that TOL essentially compares the two gradients of the volume-fraction field: $(\overline{\nabla \alpha})_{lim}$ which is the limited gradient obtained in the solution of the anti-diffusion equation, and $(\overline{\nabla \alpha})_{CD}$ which is the gradient calculated by a central difference scheme. As the interface becomes sharper after each time the anti-diffusion equation is solved, the right-hand-side of Eq. (38) decreases. Numerical experiments show that $TOL = 1$ is a suitable choice for all cases that we have considered. It is noted that the choice of $TOL = 1$ is also adopted in [37] where the anti-diffusion interface-sharpening technique is developed for incompressible two-phase flow simulations. Numerical experiments also show that the interface-sharpness is not sensitive to the choice of TOL – the interface sharpness does not vary much for TOL around 1. Too small a TOL , however, would sharpen the interface beyond the resolution limit of the underlying scheme and could introduce numerical instabilities. Typically, only 1–2 sharpening iterations are sufficient at each time step. Based on the test cases in Sections 4.1 and 4.2, the computational overhead of the interface-sharpening is found to be 5–10%.

3.4. Overall solution procedure

The solution algorithm of the two-phase compressible flow with the anti-diffusion interface sharpening for $\mathbf{U} = (\alpha, \beta, \alpha\rho^\alpha, \beta\rho^\beta, \rho\mathbf{u}, \rho E)$ from time step n to $n + 1$ can be summarized as follows:

1. Solve Eqs. (14), (15), (3)–(6) based on the flux calculated by the HLL Riemann solver for $(\alpha^{n+1'}, \beta^{n+1'}, (\alpha\rho^\alpha)^{n+1'}, (\beta\rho^\beta)^{n+1'}, (\rho\mathbf{u})^{n+1'}, (\rho E)^{n+1'})$ where $(\cdot)^{n+1'}$ indicates the variable at time step $n + 1$ without interface sharpening.
2. Solve Eqs. (16) and (17) for $(\alpha^{n+1'}, \beta^{n+1'}, (\alpha\rho^\alpha)^{n+1'}, (\beta\rho^\beta)^{n+1'}, (\rho\mathbf{u})^{n+1'}, (\rho E)^{n+1'})$ obtained here is the base solution of the flow variables without interface sharpening at time step $n + 1$.
3. Solve Eqs. (18)–(21) for α^{AD} . After each time α^{AD} is found, $\beta^{AD}, (\alpha\rho^\alpha)^{AD}, (\beta\rho^\beta)^{AD}, (\rho\mathbf{u})^{AD}, (\rho E)^{AD}$ are computed accordingly, calculated from the fluxes in Eqs. (24)–(26), (30) and (34).
4. The anti-diffusion sharpening is iterated until the stopping criterion Eq. (38) is satisfied. The result of step 3 $(\alpha^{AD}, \beta^{AD}, (\alpha\rho^\alpha)^{AD}, (\beta\rho^\beta)^{AD}, (\rho\mathbf{u})^{AD}, (\rho E)^{AD})$ is taken as the final solution $(\alpha^{n+1}, \beta^{n+1}, (\alpha\rho^\alpha)^{n+1}, (\beta\rho^\beta)^{n+1}, (\rho\mathbf{u})^{n+1}, (\rho E)^{n+1})$ at time step $n + 1$.

4. Numerical results

First, a 1-dimensional air-helium shock-tube problem and a 1-dimensional molybdenum-MORB shock-contact problem are considered to verify the interface sharpening method with the ideal-gas EOS and the Mie–Grüneisen EOS respectively. Then, 2-dimensional shock-bubble interactions based on the experiments of [9], and a 2-dimensional shock-contact problem are considered to verify the interface sharpening method in multiple-dimensions, and to illustrate the small-scale interface structures recovered by the interface sharpening method.

For all cases in this section the reconstruction of \mathbf{U}_L and \mathbf{U}_R is based on the van Leer MUSCL scheme [42]. A third-order TVD Runge–Kutta method is employed for the time integration. The time step for the governing equations is determined by the CFL requirement with a CFL number of 0.2. The zero fraction of one phase in another pure phase is represented as 10^{-6} at initialization of simulations.

4.1. Shock-tube problem

The one-dimensional air-helium shock tube case of [11] is considered. The domain is defined as $[0, 1]$ and discretized by 200 cells. The ideal-gas EOS is employed for the two phases and the initial condition is

$$(\rho, \mathbf{u}, p, \gamma) = \begin{cases} (1, 0, 1, 1.4) & \text{if } 0 \leq x < 0.5, \\ (0.125, 0, 0.1, 1.667) & \text{else.} \end{cases} \quad (39)$$

The results with and without the application of the anti-diffusion interface sharpening technique at $t = 0.15$ are shown in Fig. 1. The results at higher grid resolutions, 400 cells and 800 cells, are shown in the Fig. 2.

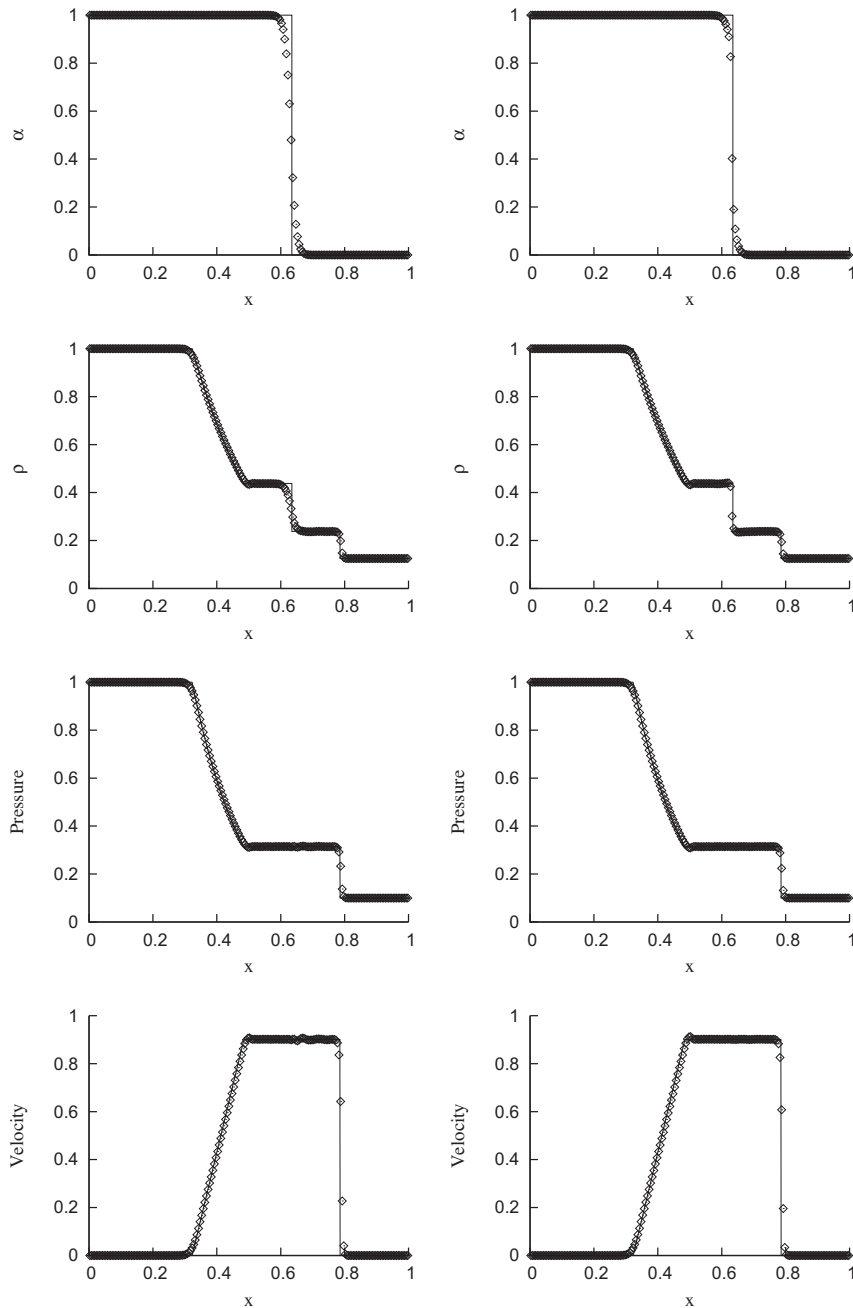


Fig. 1. Variables at $t = 0.15$ of the air-helium shock tube. Numerical results at the grid resolution of 200 cells. Symbols are the numerical results and solid lines are the exact solutions. Left column: no interface sharpening; right column: with interface sharpening.

First, the flow variables in all cases agree well with the exact solution. By comparing the results with and without the interface sharpening, one can see that the phase interface is better resolved, as represented by the reduced number of transition points in α , with the application of the anti-diffusion interface sharpening technique. Then by comparing the results with the interface sharpening at different grid resolutions, the interface is resolved by a similar number of grid points in the vicinity of the position of volume fraction 0.5, which demonstrates the interface sharpness controlled by the grid-independent stopping criterion Eq. (38). It should also be noted that the improved interface resolution also transfers to the other variables at the two-phase interface.

In order to study and compare the order of truncation error of the two-phase interface evolution with and without the application of the interface-sharpening technique, the L_1 errors and the orders of the truncation error of the volume-fraction

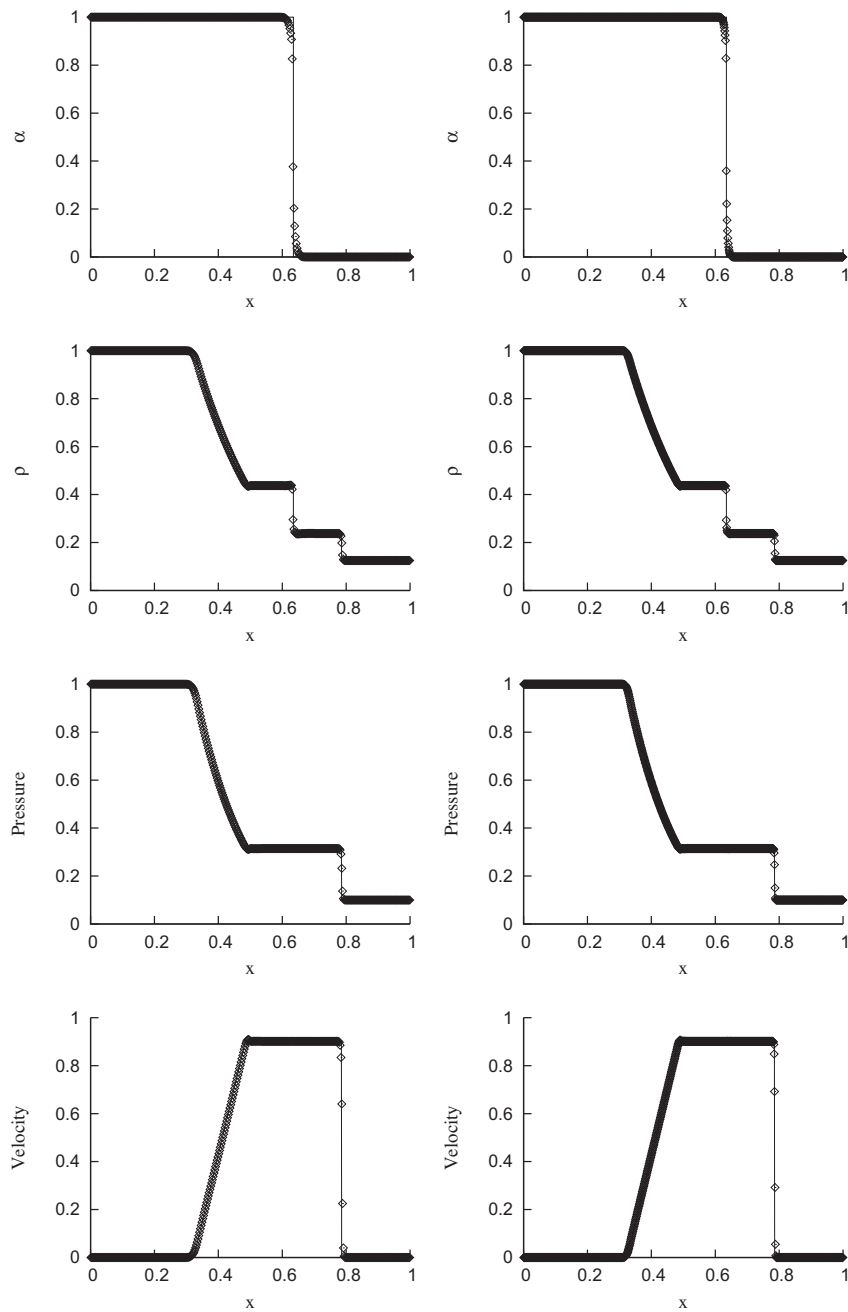


Fig. 2. Variables at $t = 0.15$ of the air-helium shock tube. Numerical results with interface sharpening. Symbols are the numerical results and solid lines are the exact solutions. Left column: grid resolution of 400 cells; right column: grid resolution of 800 cells.

Table 1

L_1 errors and orders of the truncation error at $t = 0.15$ for the air-helium shock tube.

Grid resolution	No interface sharpening		With interface sharpening	
	L_1 error	Error order	L_1 error	Error order
100 cells	0.02113		0.01571	
200 cells	0.01183	0.84	0.00729	1.11
400 cells	0.00732	0.69	0.00418	0.80
800 cells	0.00456	0.68	0.00244	0.78

field at $t = 0.15$ are calculated and shown in Table 1. The analysis indicates an error of $\mathcal{O}(\Delta x)$ for both computations with and without the application of the anti-diffusion interface-sharpening technique, and the L_1 error is reduced when the interface-sharpening technique is applied.

The exact conservation (to the 64-bit machine double precision) of the conservative variables is shown in the Table 2 for the computation at the grid-resolution of 200 cells.

4.2. 1-Dimensional shock-contact problem

The interaction of a shock wave in molybdenum and an encapsulated MORB (Mid-Ocean Ridge Basalt) liquid of [34,11] is considered. The Mie–Grüneisen EOS is employed for the two materials with coefficients

$$(\rho_0, c_0, s, \Gamma_0) = \begin{cases} (9.961, 4.77, 1.43, 2.56) & \text{for molybdenum,} \\ (2.66, 2.1, 1.68, 1.18) & \text{for MORB liquid.} \end{cases} \quad (40)$$

The domain is defined as $[0, 1]$ and discretized by 200 cells. The shock is initialized at position 0.4 and the two-phase interface at position 0.6, where the initial condition is

$$(\rho, \mathbf{u}, p) = \begin{cases} (11.042, 0.543, 30) & \text{if } 0 \leq x < 0.4, \\ (9.961, 0, 0) & \text{if } 0.4 \leq x < 0.6, \\ (2.66, 0, 0) & \text{else.} \end{cases} \quad (41)$$

The results with and without the application of the anti-diffusion interface sharpening technique at $t = 0.12$ are shown in Fig. 3. The results at grid resolutions of 400 cells and 800 cells are shown in the Fig. 4.

All flow variables in all cases agree well with the reference solutions and literature. As in the test case of the ideal-gas EOS in the Section 4.1, the phase interface is better resolved and the flow variables are consistent with the application of the anti-diffusion interface sharpening technique. The interface is resolved by a similar number of grid points in the vicinity of the position of volume fraction 0.5 at different grid resolutions as found in the Section 4.1, which demonstrates the independency of the interface-sharpening stopping criterion on the grid resolution and the case.

4.3. 2-Dimensional air-R22 shock-bubble interaction

The experimental case of a R22 cylinder in air hit by a shock wave at Mach number of 1.22 of [9] is considered to demonstrate the improvement by the interface sharpening and the recovery of the small-scale interface structures by the interface sharpening method. Results of the case have been given in a number of references employing interface capturing methods [25,22,3,6,17,20,28,38]. Corresponding to the reference literature, the configuration is considered as 2-dimensional, and the set-up of [38] and the fluid parameters of [25] are adopted here. Flow field symmetry about the streamwise center axis is assumed, and thus only the top half domain is computed. A zero-gradient boundary condition is imposed at the left and right boundaries, and the symmetry-plane boundary condition is imposed at the top and bottom boundaries. The case is computed on three levels of grid resolution in order to highlight the consistent recovery of small-scale structures as the grid resolution increases. The domain is discretized by Cartesian grids with size $\Delta x/D = \Delta y/D = 0.01$, $\Delta x/D = \Delta y/D = 0.005$ and $\Delta x/D = \Delta y/D = 0.0025$, where Δx , Δy , D are the cell sizes in x -direction and y -direction, and the bubble initial diameter. These grid sizes correspond to grid-resolutions of 100, 200 and 400 cells across the bubble diameter. Schlieren-type images, $|\nabla \rho|$, at time instants corresponding to the experimental images [9], i.e. $t = 55 \mu\text{s}$, $115 \mu\text{s}$, $135 \mu\text{s}$, $187 \mu\text{s}$, $247 \mu\text{s}$, $318 \mu\text{s}$, $342 \mu\text{s}$, $417 \mu\text{s}$ after the shock impact, are shown in Figs. 5 and 6. The enlarged images at the grid-resolution of 400 cells across the bubble diameter at $t = 247 \mu\text{s}$, $318 \mu\text{s}$, $342 \mu\text{s}$, $417 \mu\text{s}$ after the shock impact are shown in Fig. 7. The positions of the characteristic interface points and waves are recorded against time corresponding to [9,35,16] and shown in Fig. 8.

First, for the results without the application of anti-diffusion interface-sharpening, the large-scale structures and interface evolution agree well with the reference literature which confirms the validity of the underlying governing equations and numerical method. Second, with the application of interface-sharpening, the phase interface becomes significantly better

Table 2

Exact conservation (to the 64-bit machine double precision) for the air-helium shock tube at the grid resolution of 200 cells. $\sum(\cdot)$ denotes the summation of the variable over the entire computational domain. The subscripts *initialized* and *final* denote respectively the initialized state and the final state.

	No interface sharpening	With interface sharpening
$\sum(\alpha \rho^\alpha)_{\text{initialized}} - \sum(\alpha \rho^\alpha)_{\text{final}}$	$-7.10543\text{e}-14$	$-2.84217\text{e}-14$
$\sum(\beta \rho^\beta)_{\text{initialized}} - \sum(\beta \rho^\beta)_{\text{final}}$	$-1.59872\text{e}-14$	$-1.59872\text{e}-14$
$\sum(\rho E)_{\text{initialized}} - \sum(\rho E)_{\text{final}}$	$-2.27374\text{e}-13$	$-5.68434\text{e}-14$

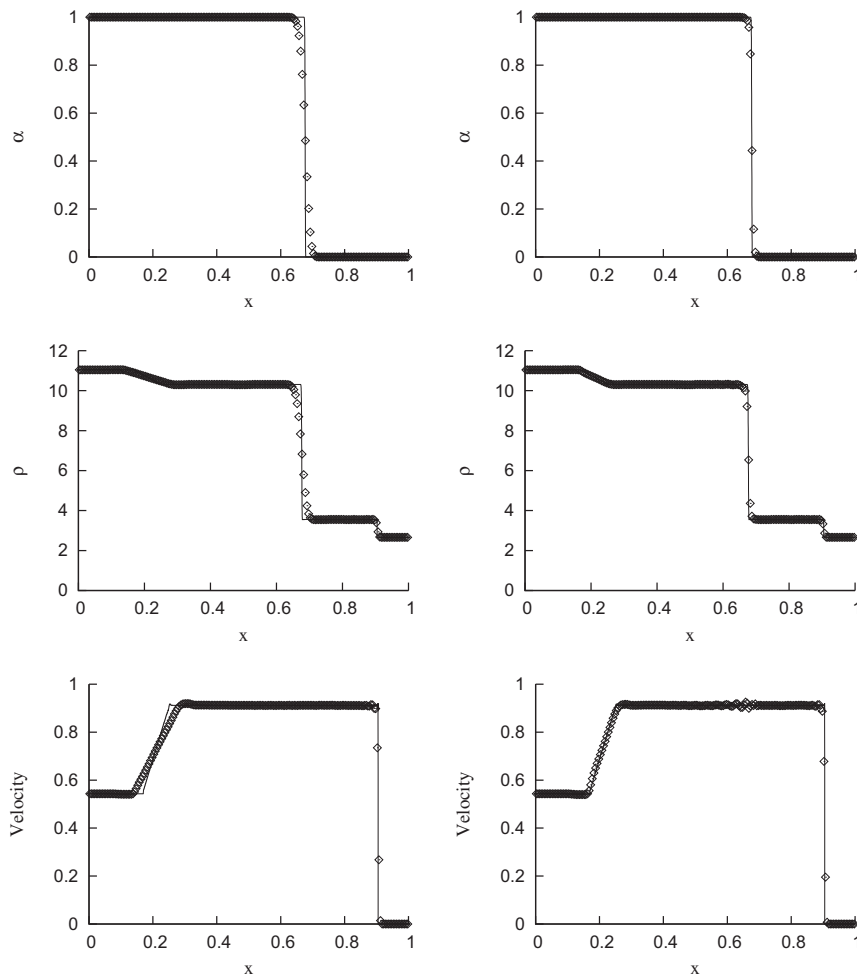


Fig. 3. Variables at $t = 0.12$ of the 1D shock-contact problem. Numerical results at the grid resolution of 200 cells. Symbols are the numerical results and solid lines are the reference solutions. Left: no interface sharpening; right: with interface sharpening.

resolved while the large-scale structures remain consistent with the reference solution where no sharpening is applied and with the reference literature. The comparison between the results with and without interface-sharpening shows that more small-scale structures are recovered by the sharpening technique. As compared to reference results obtained by adaptive mesh refinement (AMR) algorithms using interface-capturing methods [25,22,3,28] where the effective grid resolution is approximately 800 to 900 cells across the bubble diameter, the interface evolution obtained by our method agrees well with respect to prominent features of the interface roll-up present in these reference results. Our results also agree well with reference results computed by a VOF interface-tracking method [35] at a grid resolution of 400 cells across the bubble diameter. The interface instability first develops at the interface near the upper side in bubble windward direction at $t = 115 \mu\text{s}$ after the passage of the shock, and the interface rolls up at the windward side from $t = 247 \mu\text{s}$ after the shock impact onwards. The interface evolutions at $t = 318 \mu\text{s}$, $342 \mu\text{s}$, $417 \mu\text{s}$ after the shock impact clearly shows that the Kelvin–Helmholtz instability is recovered by the anti-diffusion interface-sharpening method. In particular, when we compare our results at grid resolution $\Delta x/D = \Delta y/D = 0.005$ with the reference high grid-resolution results [25,22,3,28], it can be observed that a similar interface evolution can already be recovered by the simulations with the interface sharpening on a mesh which is about 16 times coarser at the interface. One can note that the simulation of the same case in [16] computed by an anti-diffusive numerical scheme which is based on a limited downwind strategy, the interface roll-up is not recovered even for a grid with approximately 562 cells across the bubble diameter.

Third, the comparison of the numerical results at different grid resolutions shows the consistent development of the small-scale interface structures recovered by the interface-sharpening method. This is best illustrated by a comparison of numerical results at $t = 247 \mu\text{s}$, $318 \mu\text{s}$, $342 \mu\text{s}$ after the shock impact: as the grid resolution increases from $\Delta x/D = \Delta y/D = 0.01$ to $\Delta x/D = \Delta y/D = 0.005$, more small-scale interface structures are recovered; when the grid resolution further increases to $\Delta x/D = \Delta y/D = 0.0025$, even finer small-scale interface structures and fine details are recovered. While no

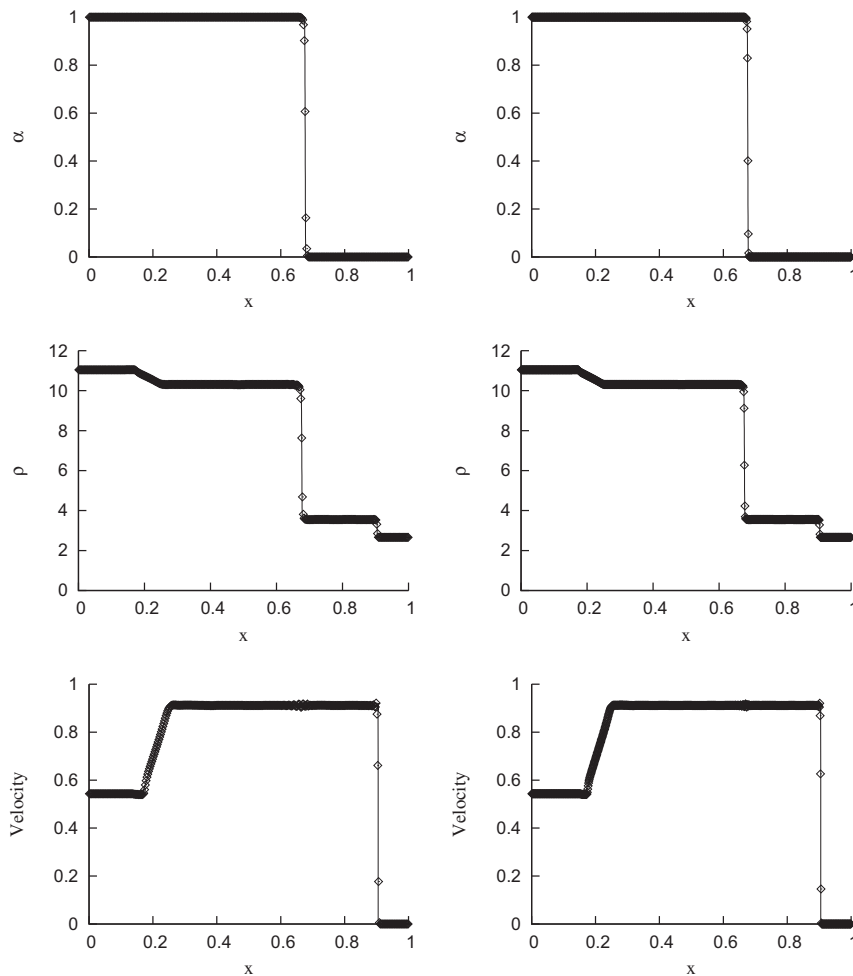


Fig. 4. Variables at $t = 0.12$ of the 1D shock-contact problem. Numerical results with interface sharpening. Symbols are the numerical results and solid lines are the reference solutions. Left column: grid resolution of 400 cells; right column: grid resolution of 800 cells.

pointwise convergence for the numerical solution of the compressible Euler equations as an initial-value problem can be expected as suggested in [30], the interface evolution with the application of the interface-sharpening technique is resolved in a consistent manner with increased recovery of small-scale structures as the grid resolution increases.

4.4. 2-Dimensional air-helium shock-bubble interaction

Another experimental case of [9] where a helium cylinder in air hit by a shock wave at Mach number of 1.22 is considered. The case has been simulated by [25,2,13,3,39,38,10,44]. While most of the results from the reference literature agree on the early-time evolution of large-scale structures, differences are observed for the evolution of small-scale structures at late times. Here we focus mainly on the early-time bubble evolution and compare our results with a high grid-resolution numerical result of [10] which is based on a wavelet-adaptive grid method that reaches an effective grid resolution of approximately 1638 cells across the bubble diameter and uses a fifth-order WENO scheme. Our numerical results are presented using a non-dimensional time \tilde{t} , which is the same as in [10] and given by $\tilde{t} = (t - t_{\text{impact}})Mc_s/r$ where t , t_{impact} , M , c_s , r are the physical time, the physical time at the shock impact, the Mach number of the shock, the sound speed of the surrounding air and the bubble initial radius, respectively.

As only the early-time evolution is considered, the domain size used in Section 4.3 is reduced in the streamwise direction and resized to $[80 \text{ mm}, -30 \text{ mm}]$ centered at the bubble center for reducing the computational effort. The same boundary conditions as those in the Section 4.3 and the fluid parameters of [38] are adopted. The case is computed at three levels of grid resolution, with grid sizes $\Delta x/D = \Delta y/D = 0.005$, $\Delta x/D = \Delta y/D = 0.0025$ and $\Delta x/D = \Delta y/D = 0.00125$, which correspond to resolutions of 200, 400 and 800 cells across the bubble diameter. The density and the vorticity fields at $\tilde{t} = 0.5, 1.0, 2.0, 4.0$ are shown in Fig. 9. The enlarged images at the grid resolution of 800 cells across the bubble

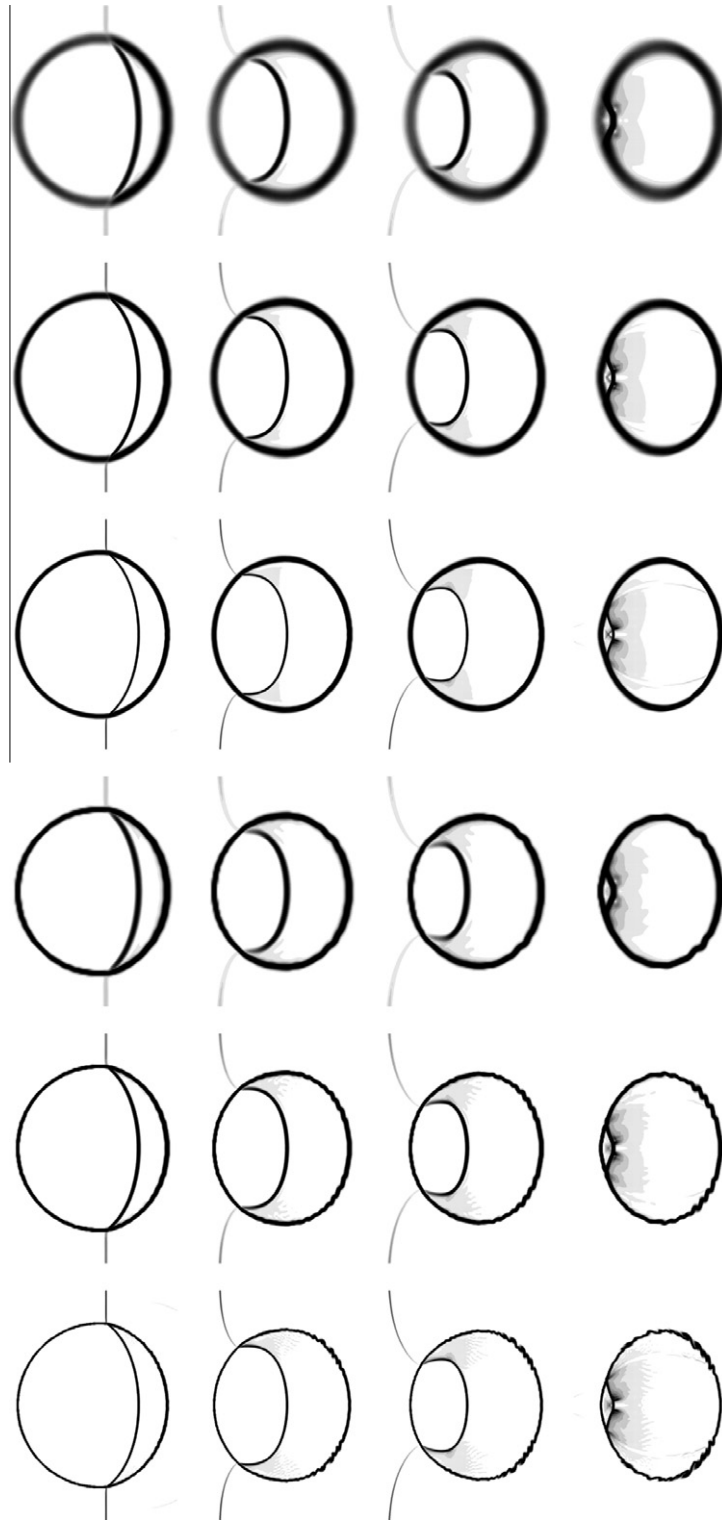


Fig. 5. Schlieren-type images, $|\nabla\rho|$, of the air-R22 shock-bubble interaction. Top 3 rows: numerical results without interface sharpening; bottom 3 rows: numerical results with interface sharpening. From top to bottom in each set: $\Delta x/D = \Delta y/D = 0.01$, $\Delta x/D = \Delta y/D = 0.005$, $\Delta x/D = \Delta y/D = 0.0025$. From left to right: $t = 55, 115, 135, 187 \mu\text{s}$ after the shock impact.

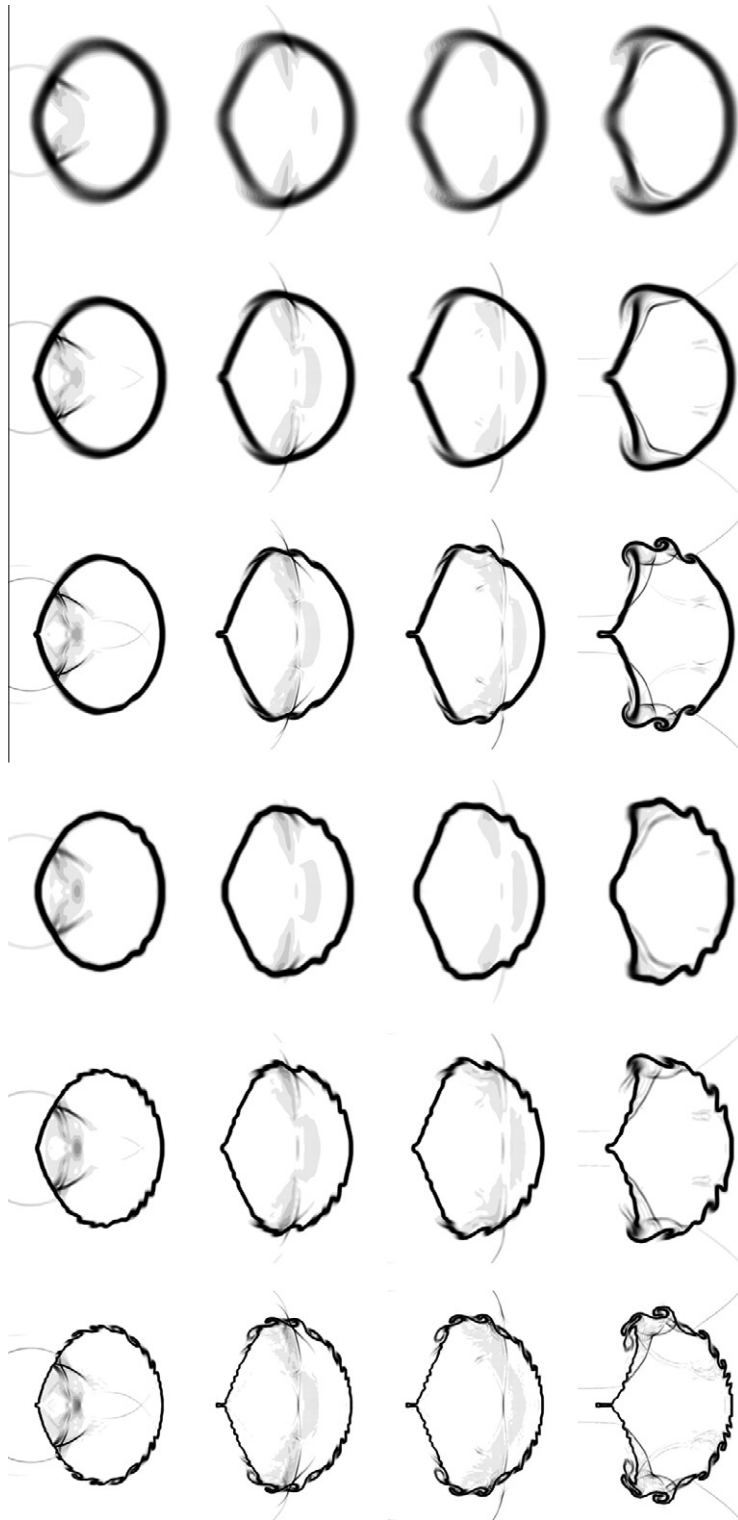


Fig. 6. Schlieren-type images, $|\nabla \rho|$, of the air-R22 shock-bubble interaction. Top 3 rows: numerical results without interface sharpening; bottom 3 rows: numerical results with interface sharpening. From top to bottom in each set: $\Delta x/D = \Delta y/D = 0.01$, $\Delta x/D = \Delta y/D = 0.005$, $\Delta x/D = \Delta y/D = 0.0025$. From left to right: $t = 247, 318, 342, 417 \mu\text{s}$ after the shock impact.

diameter at $\bar{t} = 2.0, 4.0$ are shown in Fig. 10. The positions of the characteristic interface points are recorded against time corresponding to [10] and shown in Fig. 11.

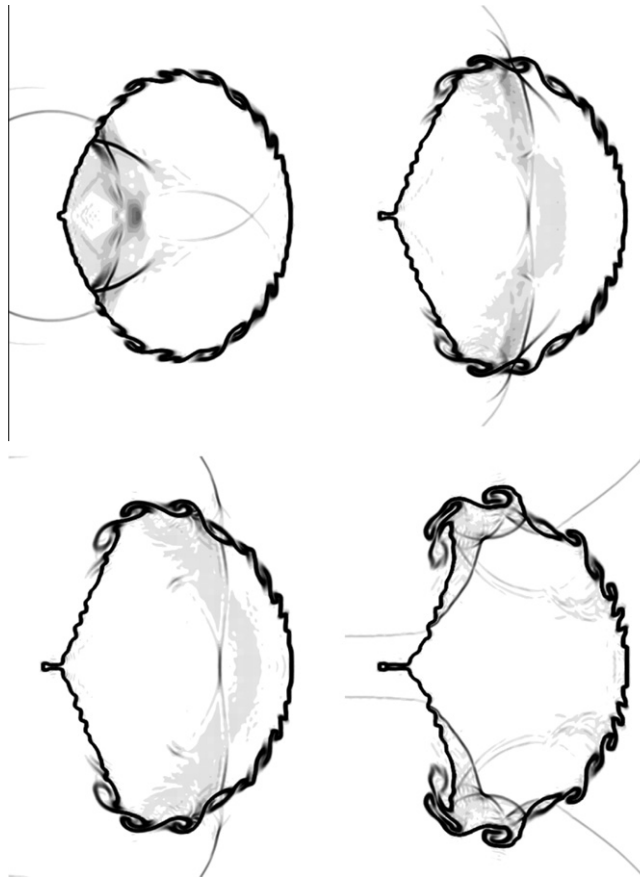


Fig. 7. Schlieren-type images, $|\nabla \rho|$, of the air-R22 shock-bubble interaction, with interface sharpening, at the grid-resolution of $\Delta x/D = \Delta y/D = 0.0025$. From left to right, top to bottom: $t = 247, 318, 342, 417 \mu s$ after the shock impact.

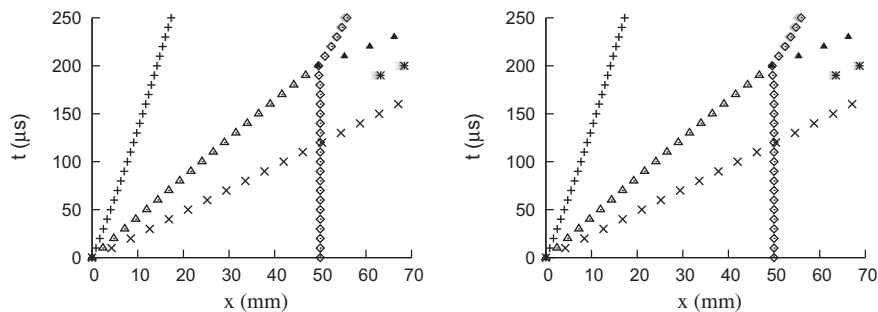


Fig. 8. Space–time diagram for the characteristic interface points and waves of the air-R22 shock-bubble interaction: '+' denotes the upstream interface, '◇' denotes the downstream interface, 'x' denotes incident shock, '△' denotes the refracted shock, '▲' and '*' denote transmitted shocks. Symbols of light grey color denote $\Delta x/D = \Delta y/D = 0.01$, symbols of dark grey color denote $\Delta x/D = \Delta y/D = 0.005$, symbols of black color denote $\Delta x/D = \Delta y/D = 0.0025$. Left: no interface sharpening; right: with interface sharpening.

Similar findings as in the Section 4.3 also apply to this test case:

- For the numerical results without the anti-diffusion interface-sharpening method the large-scale structures agree with the reference literature [10], which confirms the validity of the underlying governing equations and numerical method.
- For the numerical results with application of the interface-sharpening method the interface is better resolved, and the large-scale evolution agrees with the results without interface-sharpening and the reference literature [10].
- Finer small-scale interface structures are recovered by the interface-sharpening method. Increasingly small-scale interface structures are recovered in a consistent manner as the grid resolution increases.

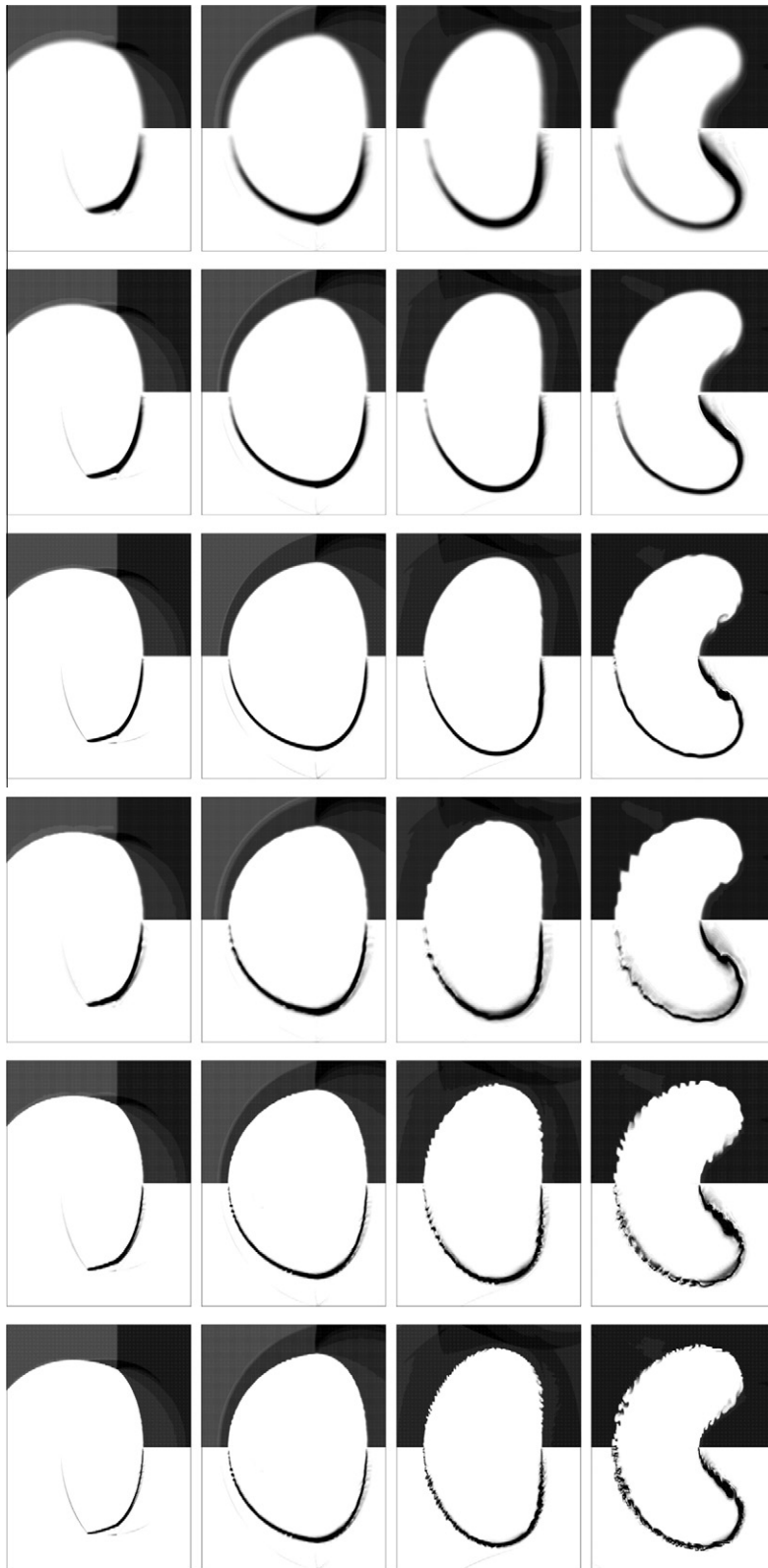


Fig. 9. Density (upper half) and vorticity (lower half) fields of the air-helium shock-bubble interaction. Top 3 rows: numerical results without interface sharpening; bottom 3 rows: numerical results with interface sharpening. From top to bottom in each set: $\Delta x/D = \Delta y/D = 0.005$, $\Delta x/D = \Delta y/D = 0.0025$, $\Delta x/D = \Delta y/D = 0.00125$. From left to right: $\hat{t} = 0.5, 1.0, 2.0, 4.0$.

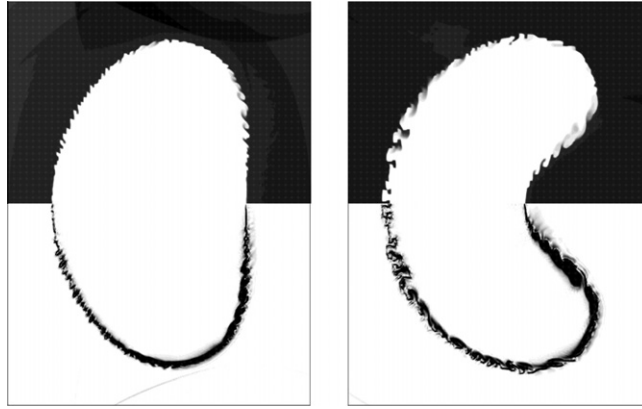


Fig. 10. Density (upper half) and vorticity (lower half) fields of the air-helium shock-bubble interaction, with interface sharpening, at the grid-resolution of $\Delta x/D = \Delta y/D = 0.00125$. From left to right: $\tilde{t} = 2.0, 4.0$.

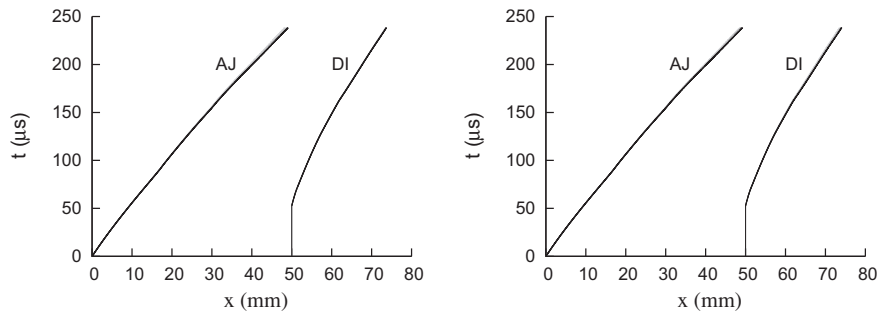


Fig. 11. Space-time diagram for the characteristic interface points of the air-helium shock-bubble interaction: 'AJ' denotes the air jet head, 'DI' denotes the downstream interface. Lines of light grey color denote $\Delta x/D = \Delta y/D = 0.005$, lines of dark grey color denote $\Delta x/D = \Delta y/D = 0.0025$, lines of black color denote $\Delta x/D = \Delta y/D = 0.00125$. Left: no interface sharpening; right: with interface sharpening. Numerical results are dimensionalized in accordance with [10].

As compared to the high-resolution results of [10] the mushroom-shaped structures due to Richtmyer–Meshkov instability [4] are recovered reliably in the numerical results with the interface-sharpening method for the grid $\Delta x/D = \Delta y/D = 0.00125$. One can note that in the simulation of the same case computed by an interface compression scheme in [33], no instability at the interface is found for a grid with resolution of approximately 225 cells across the bubble diameter.

4.5. 2-Dimensional shock-contact problem

To demonstrate the improvement by the interface sharpening method for problems with Mie–Grüneisen EOS, we consider the shock-contact problem of [19,34,35,11]. The problem is the 2-dimensional extension of the numerical case in Section 4.2 and involves a shock wave of Mach number 1.163 propagating from molybdenum to MORB liquid. Mie–Grüneisen EOS are employed for the two materials with coefficients

$$(\rho_0, c_0, s, \Gamma_0) = \begin{cases} (9.961, 4.77, 1.43, 2.56) & \text{for molybdenum,} \\ (2.66, 2.1, 1.68, 1.18) & \text{for MORB liquid.} \end{cases} \quad (42)$$

A unit square computational domain is defined, and the shock is initialized at $x = 0.35$ traveling towards the positive x -direction. MORB liquid is initialized in the region $[0.4, 0.7] \times [0, 0.5]$, and molybdenum otherwise. The dimensional reference values are 1000 kg/m^3 , 1 GPa and 1 m . The initial condition is

$$(\rho, \mathbf{u}, p) = \begin{cases} (9.964, (0, 0), 0) & \text{pre-shock molybdenum,} \\ (11.042, (0.543, 0), 30) & \text{post-shock molybdenum.} \end{cases} \quad (43)$$

A wall boundary condition is enforced at the bottom of the domain, an inflow boundary condition at the left of the domain, an outflow boundary condition with a zero gradient at the top and the right of the domain. Numerical results including the volume-fraction contours, Schlieren-type images of density and pressure, with and without the application of the

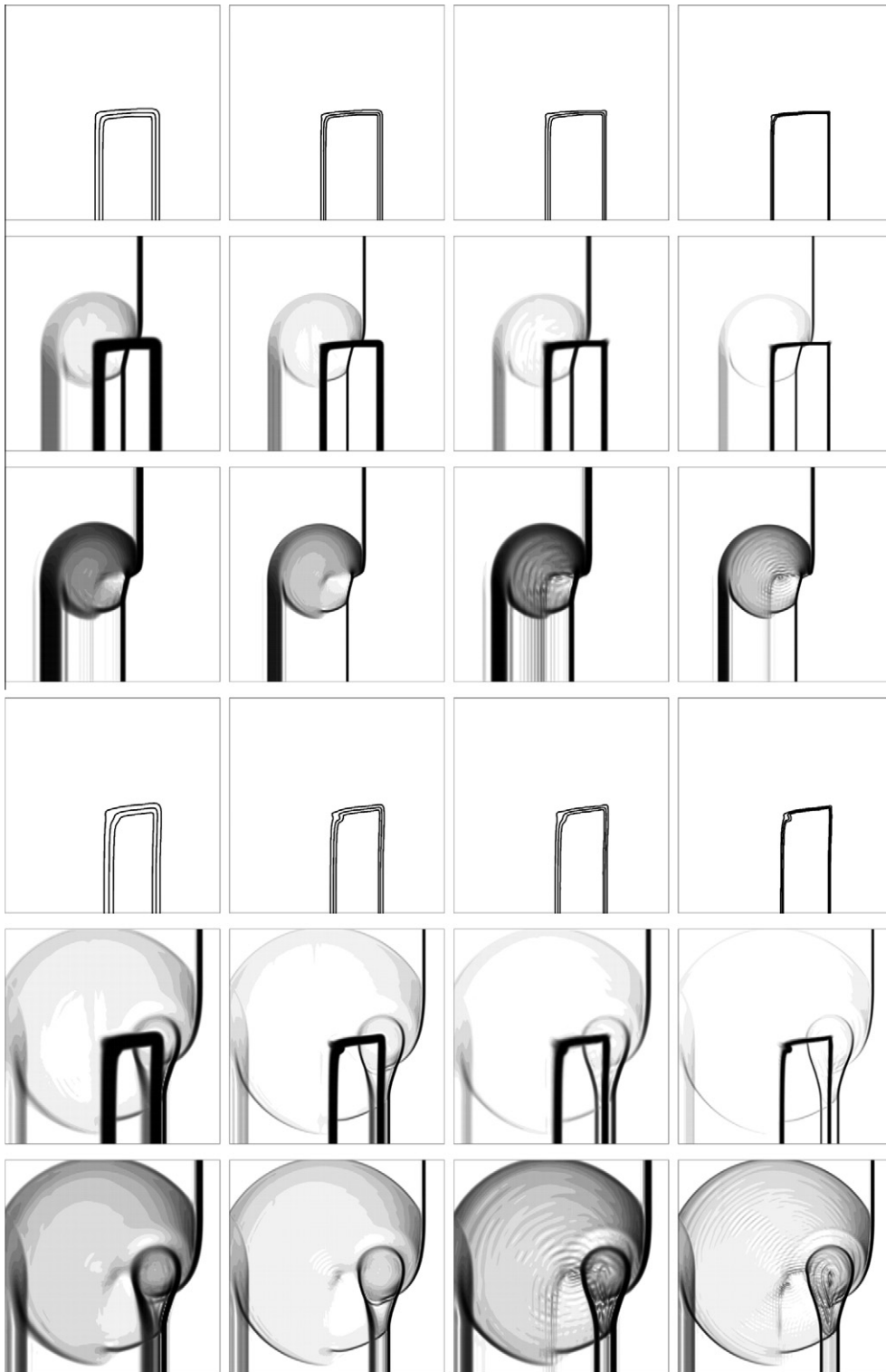


Fig. 12. Numerical results of the 2D shock-contact problem. The set of top 3 rows: $t = 50 \mu\text{s}$; the set of bottom 3 rows: $t = 100 \mu\text{s}$. From top to bottom in each set: Volume-fraction contours 0.05, 0.5, 0.95; Schlieren-type images of density; Schlieren-type images of pressure. From left to right: 200×200 (without interface sharpening), 400×400 (without interface sharpening), 200×200 (with interface sharpening), 400×400 (with interface sharpening).

interface sharpening technique, and of two grid resolutions, namely 200×200 and 400×400 are shown in Fig. 12. To emphasize weak flow features, the non-linear shading function ϕ of [25] is used for the Schlieren-type images of density and pressure. For density the function reads

$$\phi = \exp\left(-k \frac{|\nabla \rho|}{|\nabla \rho|_{\max}}\right), \quad (44)$$

where k is a constant which takes a value of 20 for this test case.

First, by comparing the volume-fraction contours of the results with and without the interface sharpening, one can note that the interface is significantly sharper when the interface sharpening is applied. The Schlieren-type images of density show that the high-speed jet at $t = 100 \mu\text{s}$ near the tip of the MORB liquid as found in [11], and in [19] computed by an AMR algorithm, is better recovered with the application of interface sharpening. The Schlieren-type images of density and pressure are also in good agreement with [35,11] at comparable grid resolutions. It should be noted that the results in Fig. 12 in [35] are not computed at the grid resolution 200×200 as described in the text but at a higher resolution [36,11].

5. Concluding remarks

In this paper an interface sharpening method based on solving an anti-diffusion equation is presented for two-phase compressible flow simulations. A conservative formulation of the Euler equations with the volume-fraction equations of [8] which are capable of simulations with the ideal-gas EOS and the Mie–Grüneisen EOS is employed as the flow governing equations. The HLL Riemann solver and the numerical method for solving the volume-fraction transport equations are described as example for the application and illustration of the interface-sharpening method. The adaptation to other Riemann solvers is straight-forward. The main concept of the interface sharpening is to solve an anti-diffusion equation for the volume-fraction field for counter-acting the numerical diffusion resulting from the underlying VOF discretization scheme. The numerical scheme for solving the anti-diffusion equation ensures the boundedness of the volume fraction and the numerical stability. The merits of the anti-diffusion interface-sharpening method are:

- No interface reconstruction is required to locate the interface.
- No interface-normal calculation and in particular no specific schemes for the interface-normal calculation as in [33] are required.
- The phase masses, momentum and energy are updated consistently in accordance with the sharpened volume-fraction field. The update of the phase masses, momentum and energy are conservative. No hyperbolic function is employed to localize the compression to the interface region for the density equation as required in [33].
- The rate of sharpening across the entire field is variable and derived from the numerical scheme of the underlying VOF discretization schemes. The interface is not compressed to a state determined based merely on the cell size regardless of the compression velocity of the interface sharpening as in [33].
- The interface-sharpening algorithm is modular and applicable to general underlying VOF discretization schemes. The interface-sharpening method can not only be applied to two-phase compressible flow simulations as shown in this paper, but also to two-phase incompressible flow simulations based on a VOF discretization, as presented and verified in [37].
- The interface-sharpening algorithm can be formulated for unstructured grids as detailed in [37]. Also, a stopping criterion for the interface-sharpening method is formulated based only on the comparison of gradients of the volume-fraction field. It does not depend on the cell size and thus is not restricted to equi-distant Cartesian grids. Thus, the entire interface sharpening method is readily applicable to underlying unstructured grid discretizations.

The anti-diffusion interface-sharpening method is verified by the numerical validation for different EOS and in 1 and 2 dimensions. Simulation results obtained by the interface-sharpening method at different grid resolutions are studied and compared with the reference literature, in particular with the reference high-resolution numerical results based on AMR algorithms. The improvements of the simulation results achieved by the anti-diffusion interface-sharpening method as shown by these test cases are:

- A good agreement of the large-scale interface structures obtained by the interface-sharpening method with the results obtained without interface sharpening, experimental results and simulation results from reference literature is observed. The interface is better resolved and finer small-scale interface structures can be recovered with the application of the interface-sharpening method.
- The recovery of finer small-scale interface structures by the interface-sharpening method consistently increases with grid resolution.
- In compressible flows involving different ideal gases where the Richtmyer–Meshkov instability and the Kelvin–Helmholtz instability are significant for the evolution of the two-phase interface, the method performs particularly well in recovering interfacial instabilities as found for the reference high-resolution numerical results based on AMR algorithms. It is noted that similar details of interface evolution are not recovered in [33,16] at comparable grid resolutions.

- Numerical cases for the Mie–Grüneisen EOS illustrate the applicability of the interface-sharpening method to different EOS with improved interface representation.

The interface-sharpening method has been implemented in the open-source package *OpenFOAM* and can be made available upon request (contact aerodynamik@tum.de with the subject line *OpenFOAM interface*).

Acknowledgment

The first author gratefully acknowledges the support by the TUM IGSS (Technische Universität München International Graduate School of Science and Engineering) for this work within the Project 3.01.

References

- [1] R. Abgrall, How to prevent pressure oscillations in multicomponent flow calculations: a quasi conservative approach, *J. Comput. Phys.* 125 (1996) 150–160.
- [2] A. Bagabir, D. Drikakis, Numerical experiments using high-resolution schemes for unsteady, inviscid, compressible flows, *Comput. Methods Appl. Mech. Eng.* 193 (2004).
- [3] J.W. Banks, D.W. Schwendeman, A.K. Kapila, W.D. Henshaw, A high-resolution Godunov method for compressible multi-material flow on overlapping grids, *J. Comput. Phys.* 223 (2007) 262–297.
- [4] M. Brouillette, The Richtmyer–Meshkov instability, *Ann. Rev. Fluid Mech.* 34 (2002) 445–468.
- [5] C.H. Chang, M.S. Liou, A robust and accurate approach to computing compressible multiphase flow: stratified flow model and AUSM⁺-up scheme, *J. Comput. Phys.* 228 (2009) 4012–4037.
- [6] A. Chertock, S. Karni, A. Kurganov, Interface tracking method for compressible multifluid, *Math. Model. Numer. Anal.* 42 (2008) 991–1019.
- [7] R.P. Fedkiw, T. Aslam, B. Merriman, S. Osher, A non-oscillatory Eulerian approach to interfaces in multimaterial flows (the ghost fluid method), *J. Comput. Phys.* 152 (1999) 457–494.
- [8] J.A. Greenough, V. Beckner, R.B. Pember, W.Y. Crutchfield, J.B. Bell, P. Colella, An adaptive multifluid interface-capturing method for compressible flow in complex geometries, *AIAA Paper* 95-1718, 1995.
- [9] J.F. Haas, B. Sturtevant, Interaction of weak shock waves with cylindrical and spherical gas inhomogeneities, *J. Fluid Mech.* 181 (1987) 41–76.
- [10] B. Hejazialhosseini, D. Rossinelli, M. Bergdorf, P. Koumoutsakos, High order finite volume methods on wavelet-adapted grids with local time-stepping on multicore architectures for the simulation of shock-bubble interactions, *J. Comput. Phys.* 229 (2010) 8364–8383.
- [11] X.Y. Hu, N.A. Adams, G. Iaccarino, On the HLLC Riemann solver for interface interaction in compressible multi-fluid flow, *J. Comput. Phys.* 228 (2009) 6572–6589.
- [12] S. Jiang, G. Ni, A second-order γ -model BGK scheme for multimaterial compressible flows, *Appl. Numer. Math.* 57 (2007) 597–608.
- [13] E. Johnsen, T. Colonius, Implementation of WENO schemes in compressible multicomponent flow problems, *J. Comput. Phys.* 219 (2006) 715–732.
- [14] A.K. Kapila, R. Menikoff, J.B. Bdzil, S.F. Son, D.S. Stewart, Two-phase modeling of deflagration-to-detonation transition in granular materials: reduced equations, *Phys. Fluids* 13 (10) (2001) 3002–3024.
- [15] S. Kawai, H. Terashima, A high-resolution scheme for compressible multicomponent flows with shock waves, *Int. J. Numer. Methods Fluids* (2010), <http://dx.doi.org/10.1002/fld.2306>.
- [16] S. Kokh, F. Lagoutiere, An anti-diffusive numerical scheme for the simulation of interfaces between compressible fluids by means of a five-equation model, *J. Comput. Phys.* 229 (2010) 2773–2809.
- [17] J.J. Kreeft, B. Koren, A new formulation of Kapila's five-equation model for compressible two-fluid flow, and its numerical treatment, *J. Comput. Phys.* 229 (2010) 6220–6242.
- [18] L.G. Margolin, Introduction to an arbitrary Lagrangian–Eulerian computing method for all flow speeds, *J. Comput. Phys.* 135 (1997) 198–202.
- [19] G.H. Miller, E.G. Puckett, A high-order Godunov method for multiple condensed phases, *J. Comput. Phys.* 128 (1996) 134–164.
- [20] G. Ni, W. Sun, A γ -DGBGK scheme for compressible multi-fluids, *Int. J. Numer. Methods Fluids* (2010), <http://dx.doi.org/10.1002/fld.2283>.
- [21] J.H.J. Niederhaus, J.A. Greenough, J.G. Oakley, D. Ranjan, M.H. Anderson, R. Bonazza, A computational parameter study for the three-dimensional shock-bubble interaction, *J. Fluid Mech.* 594 (2008) 85–124.
- [22] R.R. Nourgaliev, T.N. Dinh, T.G. Theofanous, Adaptive characteristics-based matching for compressible multifluid dynamics, *J. Comput. Phys.* 213 (2006) 500–529.
- [23] E. Olsson, G. Kreiss, A conservative level set method for two phase flow, *J. Comput. Phys.* 210 (2005) 225–246.
- [24] J.M. Picon, J.P. Boris, Vorticity generation by shock propagation through bubbles in a gas, *J. Fluid Mech.* 189 (1988) 23–51.
- [25] J.J. Quirk, S. Karni, On the dynamics of a shock-bubble interaction, *J. Fluid Mech.* 318 (1996) 129–163.
- [26] D. Ranjan, J. Oakley, R. Bonazza, Shock-bubble interactions, *Ann. Rev. Fluid Mech.* 43 (2011) 117–140.
- [27] W.J. Rider, An adaptive Riemann solver using a two-shock approximation, *Comput. Fluids* 28 (1999) 741–777.
- [28] S.K. Sambasivan, H.S. UdayKumar, Sharp interface simulations with local mesh refinement for multi-material dynamics in strongly shocked flows, *Comput. Fluids* 39 (2010) 1456–1479.
- [29] R. Samtaney, N.J. Zabusky, Circulation deposition on shock-accelerated planar and curved density-stratified interfaces: models and scaling laws, *J. Fluid Mech.* 269 (1994) 45–78.
- [30] R. Samtaney, D.I. Pullin, On initial-value and self-similar solutions of the compressible Euler equations, *Phys. Fluids* 8 (10) (1996) 2650–2655.
- [31] R. Samtaney, J. Ray, N.J. Zabusky, Baroclinic circulation generation on shock accelerated slow/fast gas interfaces, *Phys. Fluids* 10 (5) (1998) 1217–1230.
- [32] R. Saurel, F. Petitpas, R.A. Berry, Simple and efficient relaxation methods for interfaces separating compressible fluids, cavitating flows and shocks in multiphase mixtures, *J. Comput. Phys.* 228 (2009) 1678–1712.
- [33] R.K. Shukla, C. Pantano, J.B. Freund, An interface capturing method for the simulation of multi-phase compressible flows, *J. Comput. Phys.* 229 (2010) 7411–7439.
- [34] K.M. Shyue, A fluid-mixture type algorithm for compressible multicomponent flow with Mie–Grüneisen equation of state, *J. Comput. Phys.* 171 (2001) 678–707.
- [35] K.M. Shyue, A wave-propagation based volume tracking method for compressible multicomponent flow in two space dimensions, *J. Comput. Phys.* 215 (2006) 219–244.
- [36] K.M. Shyue, Private communication, 2008.
- [37] K.K. So, X.Y. Hu, N.A. Adams, Anti-diffusion method for interface steepening two-phase incompressible flow, *J. Comput. Phys.* 230 (2011) 5155–5177.
- [38] S.K. Shankar, S. Kawai, S.K. Lele, Numerical simulations of multicomponent shock accelerated flows and mixing using localized artificial diffusivity method, *AIAA Paper* 2010-352, 2010.
- [39] H. Terashima, G. Tryggvason, A front-tracking/ghost-fluid method for fluid interfaces in compressible flows, *J. Comput. Phys.* 228 (2009) 4012–4037.
- [40] C. Tomkins, S. Kumar, G. Orlicz, K. Prestridge, An experimental investigation of mixing mechanisms in shock-accelerated flow, *J. Fluid Mech.* 611 (2008) 131–150.
- [41] E. Toro, *Riemann Solvers and Numerical Methods for Fluid Dynamics*, Springer, 1997.

- [42] B. van Leer, Towards the ultimate conservative difference scheme. II. Monotonicity and conservation combined in a second-order scheme, *J. Comput. Phys.* 14 (1974) 361–370.
- [43] J. Yang, T. Kubota, E.E. Zukoski, A model for characterization of a vortex pair formed by shock passage over a light-gas inhomogeneity, *J. Fluid Mech.* 258 (1994) 217–244.
- [44] C. Wang, C.W. Shu, An interface treating technique for compressible multi-medium flow with Runge–Kutta discontinuous Galerkin method, *J. Comput. Phys.* 229 (2010) 8823–8843.